Evaluating the Representativeness of Aircraft Sampling Strategies for Cloud Water Content in LASSO Simulations over the ARM Southern Great Plains (SGP) Site

Jiakun Liang[1], William I. Gustafson Jr.[2], Dana R. Caulton[3], and Jennifer D. Small Griswold[1]

[1]Atmospheric Sciences Department, University of Hawaii at Mānoa, Honolulu, 96822, United States
[2]Atmospheric, Climate, and Earth Science Division, Pacific Northwest National Laboratory, Richland, 99354, United States
[3]Department of Atmospheric Science, University of Wyoming, Laramie, 82071, United States

Correspondence to: Jennifer Griswold (smalljen@hawaii.edu)

Abstract. Aircraft observations are widely used to evaluate cloud simulations; however, their inherently localized sampling may not fully represent the domain-scale cloud properties resolved by large-eddy simulations (LES). This study quantifies how aircraft-like sampling strategies influence the representativeness of cloud water content (CWC) derived from LES output. Using LASSO simulations for the ARM Southern Great Plains site (SGP), we emulate aircraft trajectories by prescribing multiple horizontal flight patterns (circle, diagonal, straight, combo, and zigzag) and vertical profiles (level-leg, sine wave, staircase, and zigzag) under different speed categories. Results show that sampling geometry substantially influences the degree to which aircraft-like measurements capture the magnitude and variability of domain-scale CWC. Sampling representativeness depends jointly on flight speed and trajectory geometry. For the level-leg, sine wave, and staircase vertical profiles, increasing flight speed generally improves agreement with the layer-restricted domain mean by increasing spatial coverage and reducing sensitivity to localized heterogeneity. In contrast, the zigzag pattern does not show systematic improvement with speed because its phase-locked vertical–horizontal coupling constrains effective spatial coverage. Cloud-boundary analysis further indicates the tendency to underestimate cloud-top height, while cloud-base height is more consistently captured, with higher speeds reducing both bias and variability. These findings establish a systematic framework for interpreting aircraft-based cloud measurements in the context of LES output and provide practical guidance for designing flight strategies that improve sampling representativeness in model–observation comparisons.

1 Introduction

Clouds play a fundamental role in modulating the Earth's radiative balance and hydrological cycle, yet they remain a major source of uncertainty in Earth system models (ESMs; IPCC, 2013). Differences in the representation of cloud feedbacks contribute substantially to the spread in simulated climate sensitivity (Ceppi and Nowack, 2021; Zelinka et al., 2020). Previous studies on observations and modeling found that variations in cloud fraction (CF), cloud water content (CWC), and cloud radiative properties can substantially influence the atmospheric energy budget and precipitation responses (Zelinka et

al., 2020; Wilson Kemsley et al., 2024). Evaluating and improving cloud representation in Earth system models therefore requires connecting observed cloud properties with the processes represented in the model. Observations provide constraints on cloud properties and their variability, while high-resolution simulations can provide process-level information that is difficult to obtain directly from observations alone (Stevens et al., 2005). More broadly, integrating observations with targeted high-resolution simulations has been proposed as a framework for improving the representation of unresolved processes, including cloud and convection, in Earth system models (Schneider et al., 2017). Together, these approaches provide complementary information for evaluating cloud representation across scales and for relating model biases in cloud properties to the underlying processes.

Airborne observations play a central role in cloud studies by providing spatially resolved in situ measurements that complement surface-based and satellite observations (Vogelmann et al., 2012; Wang et al., 2012; Schmid et al., 2014). Research aircraft can sample the atmosphere across both vertical and horizontal dimensions while directly measuring thermodynamic, microphysical, and chemical properties across multiple atmospheric layers (Wang et al., 2012; Schmid et al., 2014). Aircraft observations provide a complementary perspective by allowing in situ measurements within clouds and enabling targeted flight strategies, such as vertical profiling and sawtooth ascent-descent patterns, to sample cloud properties along selected three-dimensional trajectories. These measurements complement ground-based and remote-sensing observations, including active sensors that can resolve cloud vertical structure, through their ability to obtain direct measurements at selected locations within and around clouds (Wang et al., 2012). Their mobility enables sampling of evolving air masses and transitions in atmospheric conditions, supporting investigations of aerosol-cloud interactions, boundary-layer processes, and cloud evolution (McFarquhar et al., 2011; Krämer et al., 2013; Petzold et al., 2013; Schumann et al., 2013; D'Alessandro et al., 2023; Zheng et al., 2024; Zhu et al., 2024).

The U.S. Department of Energy's Atmospheric Radiation Measurement (ARM) User Facility provides long-term observations of atmospheric properties from ground-based and airborne platforms (Mather and Voyles, 2013). The ARM Aerial Facility (AAF) supports airborne field campaigns using instrumented research aircraft to obtain in situ measurements of atmospheric thermodynamic properties, aerosol and cloud properties, and trace gases over a range of altitudes and locations (Schmid et al., 2014; Mei et al., 2024). During the Holistic Interactions of Shallow Clouds, Aerosols, and Land-Ecosystems (HI-SCALE) field campaign, the ARM AAF deployed the ARM Gulfstream-1 (G-1; Gulfstream G-159) research aircraft over the Southern Great Plains (SGP) site to investigate interactions among aerosols, clouds, and land-surface processes (Fast et al., 2019). The G-1 conducted flight transects at multiple altitudes within the boundary layer and within and above clouds, providing in situ measurements of cloud and aerosol properties along targeted flight paths (Mei et al., 2024). These airborne measurements complemented the ARM ground-based observations by providing measurements at multiple altitudes and along targeted flight tracks. The AAF has supported a range of field campaigns, including HI-SCALE and ACE-ENA, and the recently integrated airborne datasets provide measurements from 236 flights conducted between 2013 and 2018 across diverse environments (Mei et al., 2024). By capturing vertical and horizontal variability at scales

unresolved by fixed observatories, AAF observations offer an essential evaluation baseline for high-resolution numerical simulations, including those from large-eddy simulation (LES) frameworks such as the LES ARM Symbiotic Simulation and Observation (LASSO) activity (Gustafson et al., 2020). The ARM Southern Great Plains (SGP) atmospheric observatory in north-central Oklahoma is one of the world's most comprehensive atmospheric sampling sites with over 30 years of continuous observation (Ackerman and Stokes, 2003; Mather and Voyles, 2013). It is located in a predominantly rural environment, with major population centers approximately 40 km away. The SGP site is influenced by a combination of anthropogenic, biogenic, and biomass-burning aerosol sources. This combination contributes to substantial horizontal and vertical variability in aerosol properties across this region. The SGP site is also well suited for studying shallow cumulus and the strong coupling between land-surface processes, boundary-layer dynamics, and cloud development (Berg and Kassianov, 2008; Berg et al., 2013; Wagner et al., 2013; Zhang and Klein, 2010, 2013). To improve understanding of these coupled processes, the HI-SCALE field campaign was conducted at the ARM SGP site in 2016 (Fast et al., 2019; Fast et al., 2022; Kulkarni et al., 2023). The campaign consisted of two 4-week intensive observational periods (IOPs): a spring IOP from April 24 to May 21, and a summer IOP from August 28 to September 23, designed to capture seasonal contrasts associated with land-surface conditions and horizontal coverage of the boundary layer and lower free troposphere. The ARM AAF deployed the G-1 research aircraft from an airport in Bartlesville, Oklahoma, approximately 130 km west of the SGP observatory (36°36'26''N, 97°29'16''W). The aircraft conducted targeted flight transects at multiple altitudes within the boundary layer and within and above clouds, providing observations over a horizontal area of approximately 100 km and altitudes ranging from about 200 to 3000 m above ground level (a.g.l) (Fast et al., 2022; Mei et al., 2024). These aircraft measurements were complemented by comprehensive ARM ground-based observations, including radars, lidars, radiosondes, radiometers, and surface flux measurements, as well as additional regional measurements from the Oklahoma Mesonet (McPherson et al., 2007; Schmid et al., 2014; Sisterson et al., 2016).

The coordinated aircraft and surface observations collected during HI-SCALE provide a dataset for characterizing aerosol properties, their vertical structure, and their interactions with shallow convective clouds over the SGP across different seasons. The flight patterns implemented during HI-SCALE also provide a useful reference for the types of aircraft sampling strategies commonly used in field campaigns over the SGP region. Furthermore, high-resolution LES ensembles such as LASSO are used to study boundary-layer cloud processes and aerosol-cloud interactions over the SGP region. The LASSO simulations analyzed in this study correspond to different cases from those sampled during HI-SCALE and are not directly constrained by the HI-SCALE aircraft observations. Instead, the HI-SCALE flight strategies serve as a practical framework for designing aircraft-like sampling trajectories within the LES domain. Aircraft observations are inherently sparse and irregular in space and time compared to gridded model domains. Evaluating the representativeness of HI-SCALE aircraft sampling relative to the LASSO simulation domain is therefore essential for robust model-data comparisons and for interpreting observational constraints on model physics. This study aims to quantify the representativeness of aircraft

sampling strategies for CWC in LASSO simulations and to assess the implications of sampling limitations for model evaluation and process understanding.

2 Data

2.1 LASSO LES Simulation

The LASSO LES framework systematically integrates routine ARM observations in a standardized, case-based structure designed to support process studies and model evaluation (Gustafson et al., 2018). LASSO provides ensembles of high-resolution simulations based on the Weather Research and Forecasting (WRF) model, constrained by ARM-derived large-scale forcing over domains centered on the SGP site. The LASSO framework has been used to investigate the sensitivity of shallow convection to large-scale forcings (Shin et al., 2021), assess cloud–land coupling in LES ensembles (Zhang et al., 2024), and examine sampling strategies for cloud radars (Oue et al., 2016), the latter being particularly relevant to the sampling-strategy focus of this study. In this study, we analyze simulations from two LASSO releases: Alpha2 and Version 1, following the standardized configurations described in the respective LASSO bundles (Gustafson et al., 2018). A consistent WRF–Thompson (Thompson et al., 2008; Thompson & Eidhammer, 2014) configuration is adopted for all analyzed cases to ensure comparability across releases.

2.1.1 LASSO Alpha2

The Alpha2 release constituted the pilot phase of the LASSO project and covered selected shallow convection case days during spring-summer 2015 and May to August 2016. The 2015–2016 cases analyzed in this study were obtained from the Alpha2 dataset. The primary objective was to demonstrate the feasibility of systematically coupling routine ARM observations with LES output in a standardized, case-based framework. For each case, an ensemble of LES driven by large-scale forcing is derived from ARM variational analysis and sounding observations and distributed together with corresponding observational datasets and performance metrics.

In contrast to later releases, Alpha2 had a more restricted scope, including fewer case days, reduced ensemble sizes, and less consistency in the applied forcing across the study period. Notably, Alpha2 included simulations performed with the WRF model. These LES were configured on a 14.4 km × 14.4 km horizontal domain centered on the SGP site, with a horizontal grid spacing of 100 m. The vertical grid spacing was approximately 30 m in the lowest ~5 km and was stretched above, with a model top near 15 km, resulting in 226 vertical levels. Simulations were generally initialized at 12 UTC and integrated for approximately 15 h, with model output archived every 10 min. Observations were bundled primarily at hourly resolution, with only limited availability of high-frequency measurements.

2.1.2 LASSO Version 1

The Version 1 release superseded Alpha2 by expanding the number of cases, standardizing the model configuration, and incorporating higher-temporal-resolution observational datasets. Version 1 comprises 30 cases in 2017, 30 in 2018, and 17 in 2019. Each case typically consists of an ensemble of approximately eight LES members. The Version 1 simulations analyzed in this study were configured over a 25 km × 25 km horizontal output domain centered on the SGP Central Facility, with a horizontal grid spacing of 100 m.

All simulations were conducted using WRF centered on the SGP Central Facility, with 100 m horizontal grid spacing. The vertical grid employed a stretched configuration, with 30 m spacing in the boundary layer and lower troposphere up to ~5 km, gradually increasing toward a model top near 14–15 km. This setup enables detailed representation of turbulent boundary layer processes and shallow cumulus clouds while retaining sensitivity to entrainment and large-scale forcings. Each simulation spanned 15 h (12–03 UTC), with output archived every 10 min. The Version 1 data are organized into three components: (1) config-obs-model, which contains forcing files, configuration metadata, skill metrics, and hourly observations; (2) raw-model, providing the full three-dimensional LES output at 10-min resolution; and (3) high-frequency observations, containing near-native resolution ARM measurements such as surface fluxes, radiation, meteorological variables. Version 1 therefore represents the first standardized long-term reference product for LASSO.

2.1.3 Model Configuration Used in This Study

A total of 91 LASSO case days are included in this study, corresponding to the case dates available in the LASSO dataset accessed for the present analysis. For each case, the analysis uses the ensemble member corresponding to a consistent WRF–Thompson configuration with large-scale forcing derived from the European Centre for Medium-Range Weather Forecasts (ECMWF) Integrated Forecast System (IFS) using the Diagnostics in the Horizontal Domains (DDH) approach, applied at the 114 km forcing scale. The DDH approach uses physical and dynamical tendencies from the ECMWF IFS to derive the large-scale forcing used in the LASSO simulations.

This intermediate forcing scale represents a balance between capturing synoptic-scale variability and avoiding excessive constraint on mesoscale and boundary-layer evolution, in contrast to the coarser 413 km and finer 16 km forcing options available in LASSO. Near-surface conditions are constrained by imposing surface sensible and latent heat fluxes from the ARM variational analysis (VARANAL) framework, which provides dynamically consistent surface fluxes and thermodynamic tendencies based on integrated ARM observations; alternative surface treatments, such as the Multiscale Data Assimilation (MSDA) approach (Gustafson et al., 2018), are available in LASSO but are not used here. Cloud microphysical processes are represented using the Thompson aerosol-aware bulk microphysics scheme, which predicts multiple hydrometeor species and has been widely applied in LES studies of shallow convection (Thompson & Eidhammer, 2014). While LASSO also includes simulations using other microphysics parameterizations, such as the Morrison double-

moment scheme (Morrison et al., 2009), and an alternative LES model, the System for Atmospheric Modeling (SAM; Khairoutdinov & Randall, 2003), this study focuses exclusively on the WRF-Thompson configuration. While a consistent WRF-based configuration is applied across cases, some aspects of the simulation forcing and boundary conditions differ among cases to account for variability in the underlying synoptic and mesoscale meteorological environments.

To minimize the influence of model spin-up on the analysis, only the later portion of each simulation was analyzed in this study. The initial 6 h following initialization were treated as spin-up, during which the boundary layer structure and cloud field adjusted to the imposed large-scale forcing (Gustafson et al., 2020). This study focuses on conditions within the same calendar day, as the final 3 h of each simulation extending into the next day were excluded from the analysis. Consequently, the analysis was restricted to the subsequent 6 h period within the same day, during which the simulated boundary layer and cloud properties are more dynamically consistent.

2.2 HI-SCALE aircraft data

This study employs the AAFMERGED dataset (Mei & Gaustad, 2024), which integrates measurements from multiple instruments operated by the AAF aboard the G-1 research aircraft. The merged dataset provides time-synchronized information on cloud microphysical properties, aerosol characteristics, thermodynamic variables, radiative quantities, and aircraft state information. However, only the aircraft latitude and longitude coordinates are used in this study. These position data are used to characterize the horizontal geometry of the HI-SCALE flight tracks. As the aircraft tracks extend beyond the LASSO model domains, the horizontal patterns are spatially scaled to the corresponding domain dimensions while retaining their characteristic geometry. The resulting trajectories are subsequently used to sample the LASSO model fields and evaluate the representativeness of different aircraft sampling strategies.

2.3 Primary Evaluation Metric

CWC is used as a proxy in this study; it is a fundamental variable for characterizing cloud microphysical structure and its interaction with radiation and precipitation processes. It is defined as the mass concentration of condensed liquid water within cloudy air and is calculated as CWC = ρq_c, where q_c is the cloud water mixing ratio and ρ is the air density. The calculated CWC was converted to g m^{-3} for the analyses presented here. The separately represented rainwater mixing ratio (q_r) is not included in the CWC analyzed here. In this study, q_c represents the cloud-water category of the Thompson microphysics scheme. CWC represents cloud-water mass per unit volume and is therefore useful for evaluating the spatial and vertical distribution of liquid water. The CWC vertical profile and its vertical integral can be used to characterize the vertical distribution and total liquid water content of clouds, respectively.

3 Methods

The aircraft-like sampling framework was designed to systematically evaluate how prescribed sampling strategies represent the evolving LASSO domain. Rather than directly replaying the original HI-SCALE flight trajectories, idealized flight paths were constructed using the observed aircraft position data as a reference for the horizontal extent and geometry of the sampling patterns. The prescribed horizontal and vertical sampling profiles were defined in model time and applied continuously during the predefined 6–12 h analysis window following the initial 6 h spin-up period. The LASSO simulations provide three-dimensional model output at 10 min intervals, whereas the aircraft position data are of 1 s resolution. To simulate aircraft-like sampling at 1 s resolution, each 10 min LASSO model output was held fixed while the prescribed trajectory advanced through the domain. Consequently, consecutive 1 s samples within a given 10 min interval represent different spatial locations within the same model state. All speed categories use the same 1 s sampling interval and 6 h analysis duration. Higher prescribed speeds increase the spatial separation between samples and the total distance covered, without changing the sampling frequency.

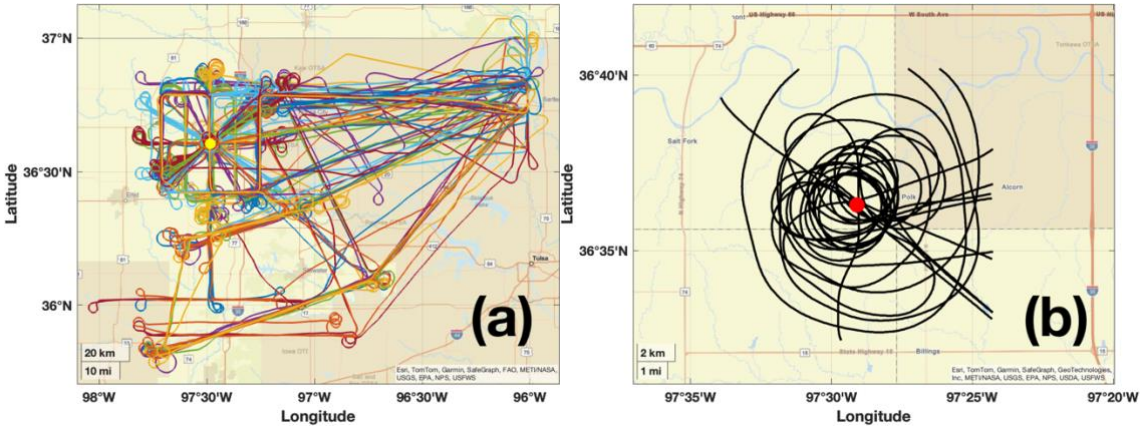
Cloud layers were identified based on a CWC threshold of 0.2 g m^{-3}, which was used to distinguish the cloud interior from the cloud–clear-air transition region (Katzwinkel et al., 2014). For each cloudy model column, cloud base was defined as the lowest model level and cloud top as the highest model level at which CWC exceeded this threshold. The diagnosed cloud base and cloud top were then used to define the vertical extent of the aircraft-like sampling trajectories. When cloud depth exceeded 200 m, sampling levels near the boundaries were offset by 100 m above cloud base and 100 m below cloud top. For cloud layers with depths of 200 m or less, these offsets were not applied. This procedure was part of the trajectory construction and was not used as an additional criterion for LASSO case selection. Thus, the in-cloud sampling duration was determined by the prescribed flight trajectory and the evolving cloud field rather than by filtering simulation cases according to a prescribed minimum in-cloud sampling time.

3.1 Aircraft Horizontal Sampling Strategies

Figure 1 shows the tracks of the flights used during the HI-SCALE campaign and the flight track used in this study. A total of 38 research flights were conducted during HI-SCALE (Figure 1a), of which 32 provided usable trajectory segments within the area corresponding to the LASSO domain and were used to derive the representative horizontal sampling patterns. Because the observed HI-SCALE tracks extend over a substantially larger horizontal area compared with the LASSO domains, the latitude–longitude patterns used in the sampling analysis were spatially scaled to the corresponding model-domain dimensions while preserving the characteristic horizontal geometries. The doubly periodic model boundaries were not used to extend the trajectories through repeated passes across the domain. In the sampling analysis, these horizontal patterns are combined with the prescribed vertical sampling strategies to construct the three-dimensional sampling trajectories through the LASSO domain.

These 32 flights were manually sorted into four types according to their different behaviors across the SGP station (circle, diagonal, straight, and combo). The circle horizontal pattern (Figure 1b) indicates the cases where the flight track is circling around the SGP station (yellow dot), which includes 6 cases. The diagonal horizontal pattern (Figure 1c) shows the tracks mainly crossing the SGP station in a diagonal manner which includes 10 cases. The straight horizontal pattern (Figure 1d) is where the aircraft track crosses the SGP site either horizontally or vertically, with 6 cases included in this pattern. The fourth observed pattern is the combo pattern (Figure 1e), which shows a comprehensive behavior with all combinations of the flight tracks around the SGP station. There are 10 cases included in this type. Figure 1f shows the zigzag pattern. Unlike the previous four patterns, which were derived directly from aircraft tracks during the field campaign, the zigzag pattern represents an idealized sampling strategy commonly used in airborne observations to enhance spatial sampling of cloud fields (Wendisch and Brenguier, 2013; Stevens et al., 2019).

The CWC sampling resulting from the four HI-SCALE-derived horizontal patterns and the idealized zigzag pattern is shown in Figure 2. During the sampling process, the horizontal patterns are applied to instantaneous outputs from the LASSO simulation for each time separately. This sampling framework retains the horizontal trajectory geometry derived from field campaign latitude–longitude information but is not intended to fully reproduce real-world flight conditions. Surface topography is not represented in the LASSO simulations, which employ a horizontally uniform lower boundary without terrain variations. The sampled data are then averaged over all time steps and across 226 vertical layers. Figure 2 shows the CWC distributions along the horizontal sampling paths. Horizontal sampling is performed separately for different LES domain sizes. The domain size is 25 × 25 km for cases from 2017 to 2019 and 14.4 × 14.4 km for cases from 2015 to 2016. The distributions for the 2017 to 2019 cases are more even than those for 2015–2016, likely due to the larger number of available cases.



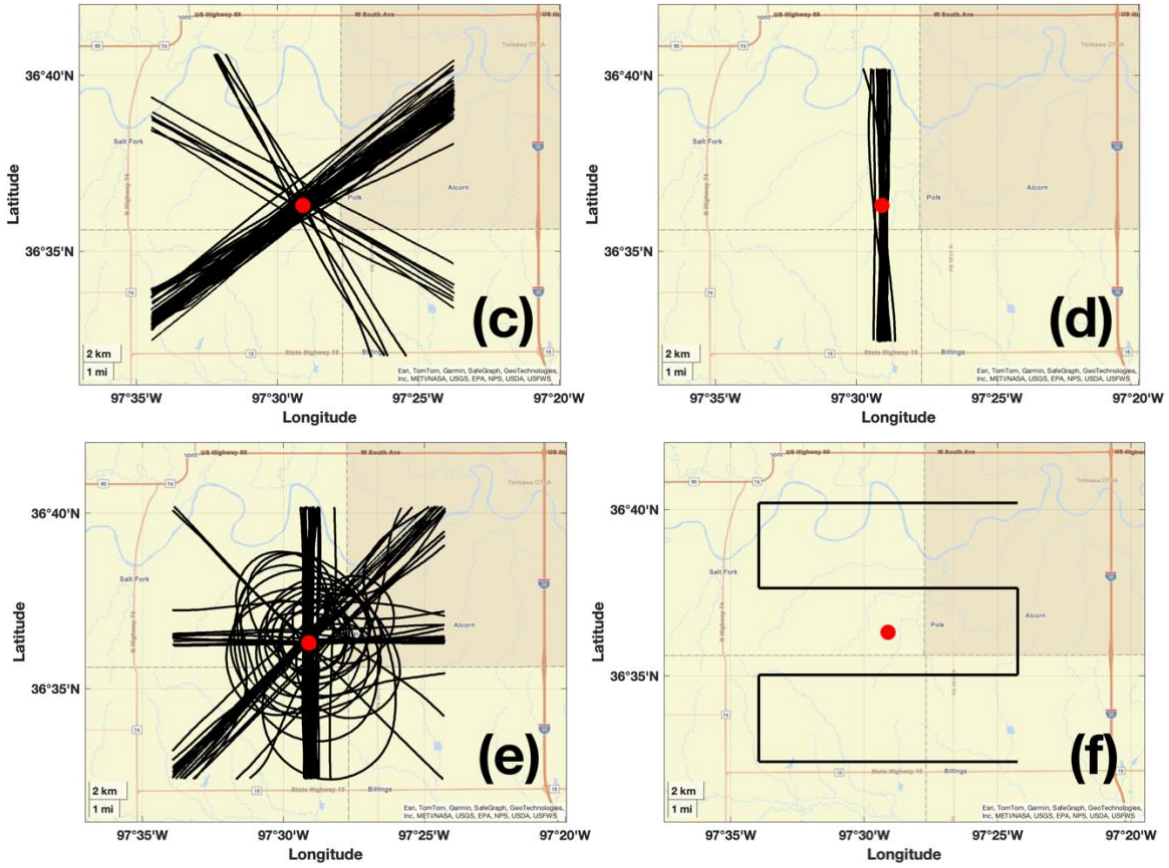
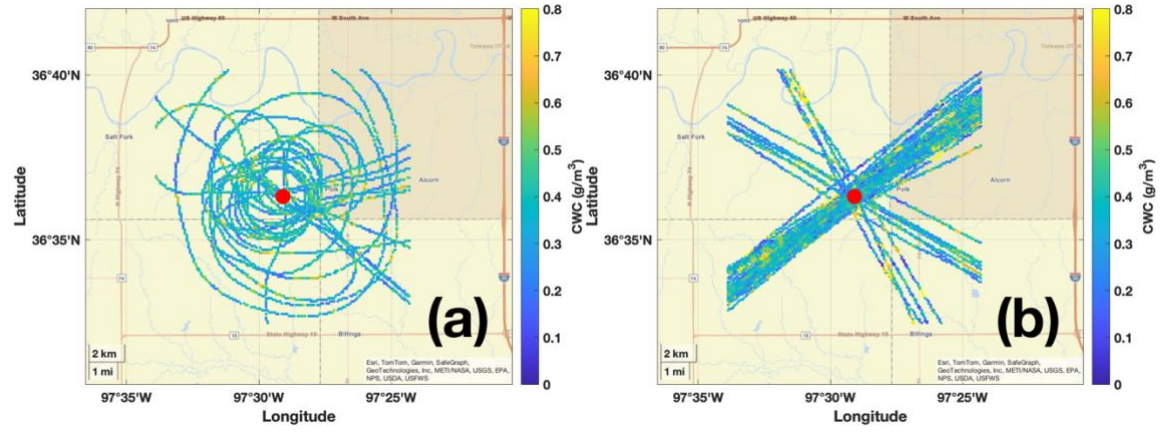


Figure 1: (a) Aircraft flight tracks from all 38 missions conducted during the HI-SCALE field campaign, with each color representing an individual flight mission. The yellow dot marks the location of the ARM SGP site. Panels (b)–(f) show zoomed-in views of representative horizontal flight patterns centered on the SGP site (red dot): (b) circle, (c) diagonal, (d) straight, (e) combo, and (f) zigzag patterns. Black lines denote the aircraft flight tracks.



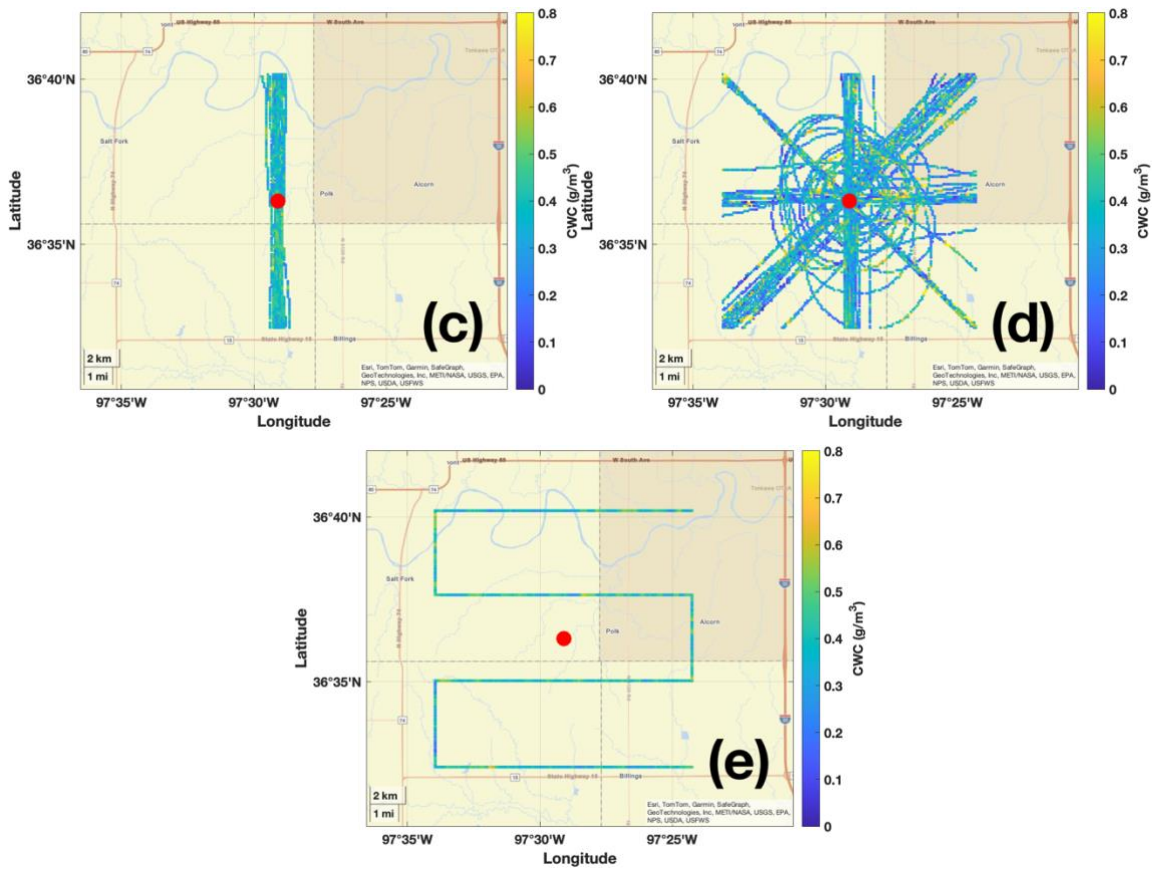


Figure 2: Height-averaged CWC sampled along the representative horizontal flight patterns: (a) circle, (b) diagonal, (c) straight, (d) combo, and (e) zigzag. For each pattern, CWC was extracted along the flight trajectory and vertically averaged within the corresponding sampling layer to emulate aircraft-based in situ measurements.

3.2 Aircraft Vertical Sampling Strategies

To enable direct comparison with the LASSO simulations, the HI-SCALE flight tracks were first categorized into four geometric types: circle, diagonal, straight, and combo as mentioned above. The vertical sampling strategies were manually designed following three canonical flight patterns including level-leg, sine wave, and staircase, which have been widely adopted in cloud observational studies to characterize vertical cloud structure and variability (Gerber et al., 2005, 2013; Brenguier et al., 2013). These patterns are considered complementary as horizontal legs at fixed altitudes provide robust statistics at specific cloud levels, while vertically varying profiles capture gradients in thermodynamic and microphysical properties within clouds (Wang & Sassen, 2001; Gerber et al., 2005; Wendisch and Brenguier, 2013). The use of multiple vertical sampling modes is a long-standing observational practice in field campaigns, including ARM and DOE-supported aircraft missions, to balance vertical coverage, temporal continuity, and statistical representativeness of in-cloud measurements. In this study, the vertical sampling profiles were constructed using cloud-base and cloud-top information

diagnosed from the LASSO simulations. The specific implementation differs among the sampling strategies, as described below.

Previous studies have shown that measurements obtained near cloud boundaries often differ from interior-cloud values due to entrainment and enhanced variability in microphysical properties (Passer et al., 2025; Gryspeerdt et al., 2022). To reduce sampling directly at cloud boundaries, 100 m offsets from the diagnosed cloud base and cloud top were applied where the cloud depth exceeded 200 m. For shallower cloud layers, these offsets were not applied.

For the level-leg profile, three fixed sampling altitudes were defined for each LASSO case based on the mean diagnosed cloud-base, mid-cloud, and cloud-top heights over the 6 h analysis period. The lower and upper legs were set 100 m above the diagnosed cloud base and 100 m below the diagnosed cloud top, respectively, and the middle level was defined as the midpoint between the diagnosed cloud-base and cloud-top heights. The trajectory progressed successively from the lower to the middle and upper sampling levels. Transitions between adjacent levels were represented by linear changes in altitude over 10 min, while the trajectory continued to advance horizontally. The sine wave profile was constructed using a continuous sine waveform, with wave crests corresponding to 100 m below cloud top and troughs to 100 m above cloud base, enabling repeated sampling across the cloud depth within a single transect. The staircase profile was constructed similarly but uses three discrete altitude levels, with the aircraft flying successively near the cloud top, mid-cloud, and cloud base for approximately 10 minutes at each level, again applying the same altitude offsets. These three profiles provide complementary perspectives on cloud vertical heterogeneity: the level-leg pattern emphasizes quasi-horizontal variability, the sine wave track resolves continuous vertical gradients, and the staircase profile combines vertical sampling with temporally stable measurements, a balance commonly employed in aircraft-based cloud process studies (Gerber et al., 2005).

In addition to the separable horizontal–vertical sampling combinations described above, a zigzag trajectory was constructed as a distinct three-dimensional flight configuration. Unlike the level-leg, sine wave, and staircase profiles, which prescribe vertical variation independently of horizontal pattern type, the zigzag design integrates horizontal tracks and cloud-relative vertical transitions into a single structured pathway. Similar zigzag flight patterns have been widely employed in aircraft cloud-process studies to repeatedly sample cloud layers and resolve vertical variability (Gerber et al., 2013; Savelyev et al., 2018; Dorff et al., 2025). As illustrated in Figure 3d, the aircraft performs successive horizontal legs across the LES domain while alternating among cloud base (+100 m), mid-cloud, and cloud top (−100 m) levels. Vertical transitions occur at the turning points between horizontal legs, forming a repeating stacked sequence of cloud-relative sampling levels. The altitude of each leg is diagnosed locally along the trajectory based on instantaneous cloud properties, consistent with the vertical profile construction described above, so that cloud base and cloud top heights vary spatially and temporally according to the evolving model state.

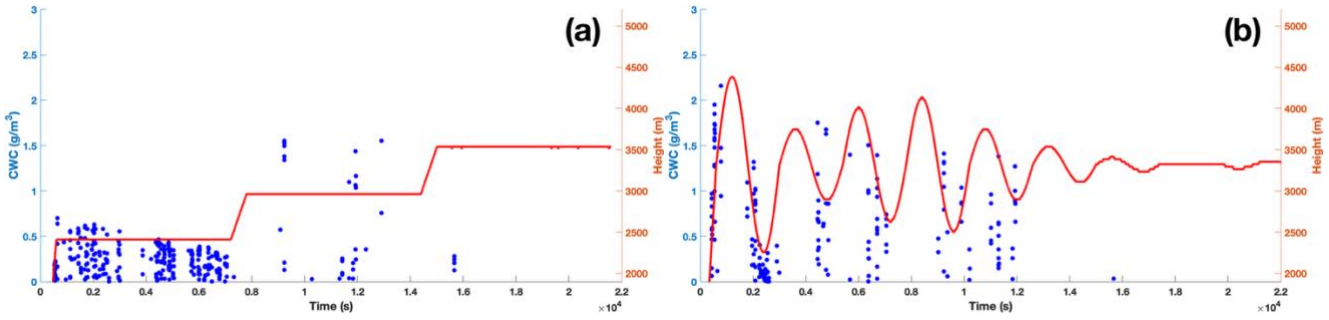
3.2.1 Vertical Sampling Strategies and Their Implementation

Four different vertical profiles are employed in this study (shown in Figure 3): level-leg, sine wave, staircase, and zigzag. The June 9, 2015 case is used as an illustrative example to show the prescribed sampling trajectories. Figure 3 shows the CWC sampling along these four profiles under the moderate-speed category. The sampled CWC exhibits a distinctly intermittent structure, characterized by clusters of elevated values separated by intervals of near-zero CWC. The CWC sampling is concentrated into vertically aligned groupings in time rather than forming a continuous spread, which reflects the episodic nature of in-cloud sampling that could be found when the real aircraft repeatedly enters and exits cloud volumes along its flight path.

The vertical profile of altitude (red line) indicates that periods of enhanced CWC systematically coincide with the sequence of ascent and descent altitude ranges for cloud layers, especially for sine wave and staircase vertical profiles. Low or negligible CWC values correspond to flight segments outside cloud boundaries. The apparent vertical alignment of CWC clusters in time therefore arises from the aircraft traversing cloud layers over finite vertical extents, during which sustained in-cloud conditions are sampled across multiple consecutive measurements.

This distribution also reflects the combination of aircraft motion through the cloud field and the horizontal and vertical gradients in CWC near cloud boundaries. Within each 10 min LASSO output interval, the model field remains fixed while the prescribed trajectory continues to advance horizontally and vertically. Consequently, consecutive 1 s samples represent different spatial locations within the same model state, which can produce temporally clustered CWC values when the trajectory passes through regions of enhanced cloud water.

Together, the sampled CWC distribution is consistent with repeated crossings of vertically confined cloud structures, such as shallow convective clouds over the SGP station, rather than continuous sampling within a single, horizontally extensive cloud. The alignment between CWC enhancements and altitude variations illustrates how the prescribed trajectory samples different parts of the simulated cloud field, including both in-cloud and out-of-cloud sampling periods.



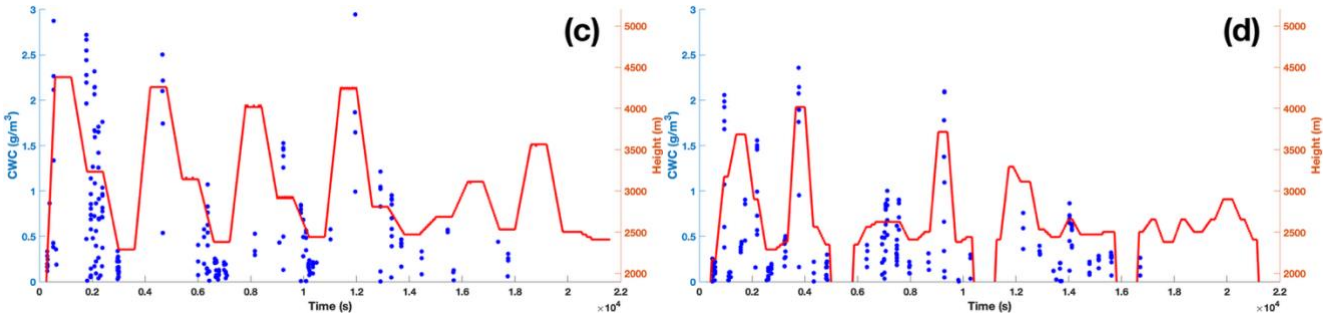


Figure 3: Time series of sampled CWC (blue dots) for four vertical flight profiles under the moderate speed category for the June 9, 2015, case. Panels (a)–(c) correspond to the level-leg, sine wave, and staircase vertical profiles, respectively, each employing the circle horizontal pattern, while panel (d) shows the zigzag profile. The red line denotes the aircraft altitude vertical trajectory (height as a function of time), and blue dots represent the CWC sampled along the flight path at each time step.

3.3 Speed Categories

The idealized flight patterns were further interpreted in terms of characteristic aircraft operating speeds. Research aircraft were grouped into three categories according to their typical true airspeed during the atmospheric field sampling. Low-speed aircraft (approximately 30−100 m s^{-1}), such as the de Havilland Twin Otter (DHC-6), are capable of stable flight and fine-scale vertical maneuvering, making them well suited for detailed boundary layer and cloud-scale sampling. Moderate-speed aircraft (approximately 100–170 m s^{-1}) include the ARM G-1 aircraft (Schmid et al., 2014), which was used during the HI-SCALE campaign, the C-130/LC-130, Beechcraft 200 (King Air), and British Aerospace 146 (BAe-146; Sánchez-Marroquín et al., 2019). These platforms provide a balance between spatial coverage and sampling resolution and are commonly employed for mesoscale process studies. High-speed platforms (approximately 200–250 m s^{-1}), such as the NASA Douglas DC-8 and NASA WB-57, are typically used for missions requiring rapid regional coverage or sampling of the upper troposphere and lower stratosphere. Based on these characteristic speed regimes, nominal speeds of approximately 33, 100, and 200 m s^{-1} were prescribed for the slow, moderate, and fast trajectories, respectively. The moderate speed was based on the characteristic G-1 research speed of approximately 100 m s^{-1} (Schmid et al., 2014), while the slow and fast trajectories correspond to approximately one-third and twice the reference speed, respectively. Framing the sampling trajectories in terms of these speed regimes clarifies how the prescribed horizontal-vertical profile combinations relate to realistic aircraft operations and facilitates interpretation of sampling representativeness across different classes of airborne observations.

The prescribed aircraft speeds also determine the horizontal distance traveled between consecutive 1-s sampling positions. For the 100-m horizontal grid spacing used in the LASSO simulations, a speed of 100 m s^{-1} corresponds approximately one grid spacing per 1-s sampling interval, whereas slower or faster aircraft traverse less or more than one grid spacing between consecutive samples. This does not require a one-to-one correspondence between aircraft samples and model grid cells. Rather, it determines the spatial separation between consecutive trajectory positions and the extent of the model domain traversed during a fixed sampling period.

The aircraft-like sampling strategy combines horizontal patterns derived from HI-SCALE observations with prescribed vertical profiles and characteristic aircraft speed categories. Although the Alpha2 and Version 1 simulations differ in horizontal domain size, the same vertical-profile design is applied to both datasets. The low-, moderate-, and high-speed categories provide a practical framework for examining how trajectory geometry influences the representativeness of aircraft-like measurements within the LES domain.

3.4 Three-Dimensional Sampling Trajectory

Figure 4 shows the simulated CF for June 9, 2015, together with the prescribed sampling trajectory. CF is used here to visualize the three-dimensional cloud structure and spatial distribution within the LES domain. The designed flight track is constructed independently of the simulated CF distribution. As a result, the trajectory may intersect regions with different CF according to the spatial heterogeneity of the simulated cloud field. As the prescribed trajectory moves horizontally and vertically through the domain, it samples both cloud and less-cloudy regions and may cross cloud boundaries. Figure 4 therefore illustrates how the aircraft-like sampling trajectory intersects the simulated cloud field in three dimensions for this example case.

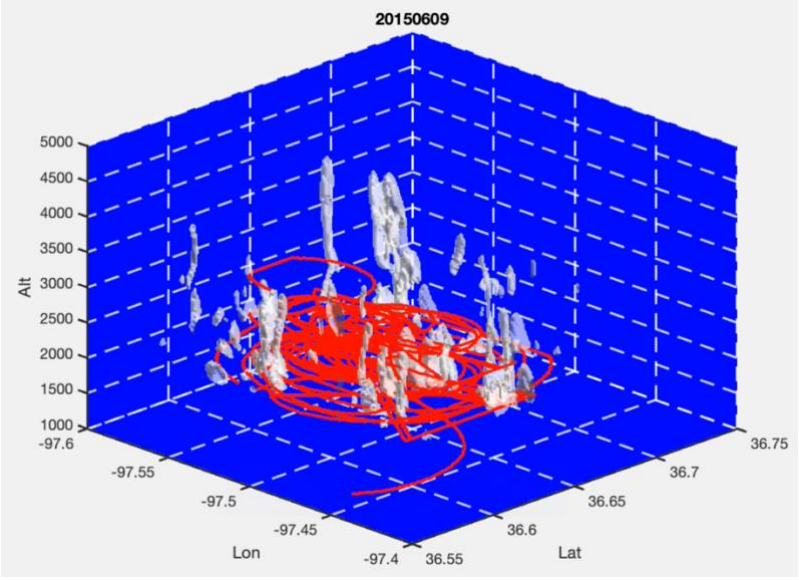


Figure 4: Three-dimensional CF for the June 9, 2015, case within the 14.4 km × 14.4 km model domain, shown together with the prescribed sampling trajectory. The red curve denotes the prescribed sampling trajectory combining the circle horizontal pattern with the level-leg vertical profile under the moderate speed category.

4 Results

4.1 Spatial Distribution of Regression Slopes Across Sampling Configurations

To assess the representativeness of aircraft-like sampling relative to the model domain, trajectory-averaged CWC is compared with the corresponding domain mean computed over only the vertical layers intersected by the flight path. Aircraft observations provide spatially limited samples of heterogeneous cloud fields. Their representativeness can depend on the sampling strategy and the spatial scales over which the observations are interpreted (Field et al., 2016; Schutgens et al., 2017). Restricting the domain average to the sampled layers ensures a consistent spatial reference as the trajectory-derived and domain-mean CWC represent the same vertical portion of the simulated cloud field. The domain mean is therefore used here as a domain-scale reference for quantifying sampling representativeness rather than an observational reference.

Figure 5 shows an example of the sampled CWC values. Scatterplots for all trajectory configurations and speed categories are provided in the Supplemental Material (Figure S1). For each trajectory configuration, paired sampled and domain-mean CWC values are calculated separately for each 10-min model-output interval within the 6 h analysis period. The regression is calculated across all cases, with the selected ensemble member for each case. The color distribution indicates that the relationship between CWC and sampling height is not uniform across the sampled trajectories. Although the Spearman's rank correlation between domain-mean CWC and sampling height is moderately positive (r = 0.609), the corresponding trajectory-averaged CWC shows substantially weaker and more variable relationships across sampling strategies and aircraft speeds. This difference suggests that the vertical variation in the domain-scale CWC is not consistently represented by individual aircraft-like trajectories, which are also affected by horizontal cloud heterogeneity and the spatial sampling imposed by the flight path.

The regression slope derived from the linear fit between sampled and domain-mean CWC quantifies how well the aircraft-like sampling reproduces the magnitude of domain-scale CWC. Slope values close to 1 indicate better agreement in amplitude between the sampled and domain-mean CWC. Figure 5 serves as an example of this calculation. This procedure is systematically applied to all combinations of horizontal patterns, vertical profiles, and speed categories. The statistics summarized below are calculated across the analyzed cases from both LASSO domain configurations. A separate comparison by domain size did not show a systematic reduction in sampling representativeness for the larger domain, although the effects of domain size cannot be isolated quantitatively from differences among simulation years and LASSO releases. Figure 6 summarizes the resulting slope values across configurations, providing an integrated assessment of sampling representativeness under varying trajectory geometries and flight speeds.

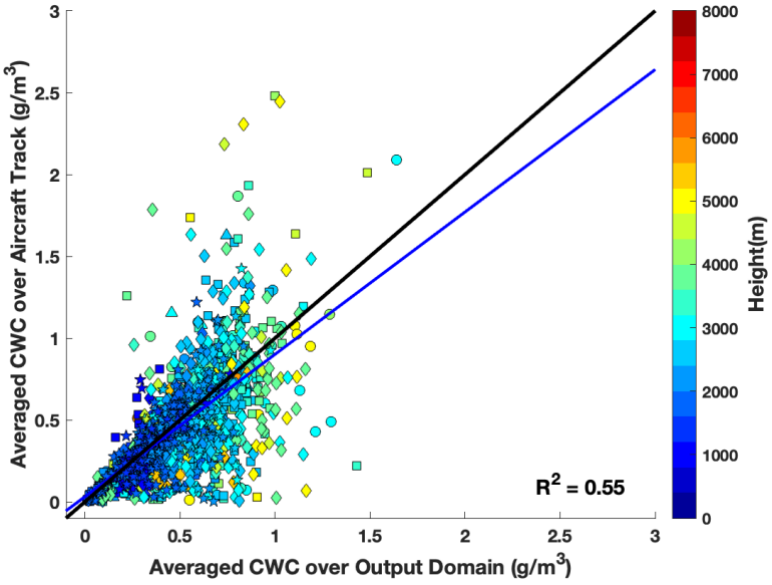


Figure 5: Scatter plot comparing aircraft-sampled and domain-averaged CWC, using the circle horizontal pattern, level-leg vertical profile, and moderate speed category. The x-axis represents the domain-mean CWC calculated over only the vertical layers intersected by the aircraft trajectory, while the y-axis shows the CWC averaged along the corresponding flight track. Colors indicate sampling height (m). The black line denotes the 1:1 reference line, and the blue line shows the linear regression fit.

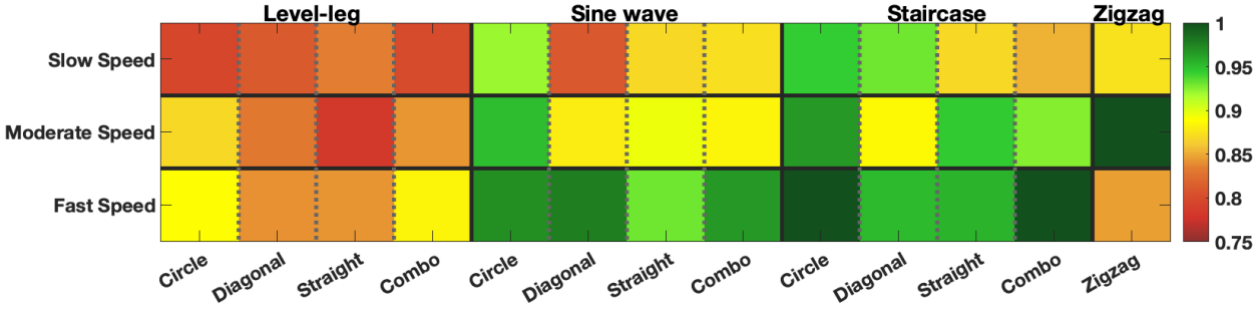


Figure 6: Regression slope values between track-averaged CWC and domain-mean CWC computed over corresponding relative vertical layers, shown for all combinations of vertical patterns, horizontal patterns, and flight-speed categories. Slope values near unity (green) indicate strong agreement between track-sampled and domain-averaged CWC and therefore high representativeness, whereas lower values (red) reflect reduced agreement.

For the level-leg, sine wave, and staircase vertical patterns, representativeness generally improves with increasing flight speed. Within the present sampling framework, higher prescribed speed increases the spatial extent traversed by the trajectory during each fixed model-output interval, reducing sensitivity to localized cloud variability and generally improving agreement with the domain-scale field. Among these vertical patterns, the staircase profile exhibits the most consistent agreement, with regression slope values exceeding 0.85 across all horizontal patterns and speed categories. For the staircase profile combined with the circle horizontal pattern, the slope increases from 0.94 at slow speed to 0.97 at moderate speed and approaches unity under the fast speed category. In contrast, the level-leg profile shows the largest deviation, ranging from approximately 0.78 to 0.89. The sine wave profile yields slopes ranging from approximately 0.81 to 0.98.

The statistical metrics summarized in Table 1 provide a quantitative assessment of sampling representativeness. Correlation coefficients (r) for the level-leg, sine wave, and staircase profiles generally range from about 0.57 to 0.83 across the trajectory patterns and speed categories, indicating moderate to strong agreement between sampled and domain-mean CWC. Among these profiles, the staircase profile shows relatively consistent performance, with r values ranging from 0.60 to 0.83 across the horizontal patterns and speed categories. The highest correlation among these profiles is 0.83 for the staircase pattern under the fast-speed category, while the lowest is 0.57 for the level-leg profile with the diagonal pattern at slow speed. Normalized RMSE (nRMSE) values range from approximately 0.45 to 0.66 for level-leg, sine wave, and staircase profiles, while normalized bias (nBias) remains small, ranging from –0.17 to –0.01, indicating limited systematic deviation between sampled and domain averages. In contrast, the zigzag pattern shows greater variability across speed categories, with r ranging from 0.37 to 0.74, nRMSE from 0.76 to 1.27, and nBias from –0.13 to 0.20. Overall, the statistical metrics show that agreement with the domain mean generally improved with increased flight speed for the level-leg, sine wave, and staircase profiles within the present sampling framework, while geometrically constrained patterns such as zigzag exhibit less consistent behavior.

Table 1. Statistical metrics describing the sampling representativeness based on comparisons between sampled averages and domain-mean values.

Level-leg												
	Circle			**Diagonal**			**Straight**			**Combo**		
Speed Category	Slow	Moderate	Fast	Slow	Moderate	Fast	Slow	Moderate	Fast	Slow	Moderate	Fast
r	0.61	0.74	0.79	0.57	0.74	0.74	0.61	0.65	0.73	0.59	0.74	0.79
nBias	-0.11	-0.06	-0.04	-0.11	-0.09	-0.09	-0.11	-0.10	-0.07	-0.11	-0.07	-0.03
nRMSE	0.54	0.48	0.45	0.57	0.45	0.46	0.54	0.49	0.48	0.55	0.46	0.45
Sample mean (g m^{-3})	0.39	0.42	0.45	0.39	0.42	0.42	0.39	0.40	0.43	0.38	0.43	0.46
Sample STD (g m^{-3})	0.28	0.29	0.31	0.29	0.28	0.29	0.29	0.27	0.29	0.28	0.29	0.31
Domain mean (g m^{-3})	0.44	0.45	0.47	0.44	0.46	0.46	0.43	0.45	0.46	0.43	0.46	0.48
Domain STD (g m^{-3})	0.21	0.23	0.25	0.21	0.23	0.24	0.21	0.22	0.23	0.20	0.24	0.25
Sine wave												
	Circle			**Diagonal**			**Straight**			**Combo**		
Speed Category	Slow	Moderate	Fast	Slow	Moderate	Fast	Slow	Moderate	Fast	Slow	Moderate	Fast
r	0.74	0.75	0.78	0.60	0.71	0.77	0.64	0.73	0.78	0.62	0.74	0.80
nBias	-0.12	-0.09	-0.08	-0.17	-0.12	-0.10	-0.13	-0.13	-0.10	-0.14	-0.12	-0.07
nRMSE	0.53	0.54	0.52	0.62	0.57	0.52	0.65	0.55	0.51	0.65	0.53	0.50
Sample mean (g m^{-3})	0.39	0.44	0.47	0.38	0.43	0.46	0.40	0.41	0.43	0.39	0.43	0.47
Sample STD (g m^{-3})	0.36	0.36	0.38	0.34	0.36	0.38	0.36	0.35	0.35	0.36	0.34	0.37
Domain mean (g m^{-3})	0.46	0.48	0.51	0.46	0.49	0.51	0.46	0.47	0.48	0.46	0.49	0.50

Domain STD ($g\ m^{-3}$)	0.25	0.27	0.29	0.25	0.27	0.28	0.25	0.27	0.27	0.25	0.27	0.28

Staircase

	Circle			**Diagonal**			**Straight**			**Combo**		
Speed Category	Slow	Moderate	Fast	Slow	Moderate	Fast	Slow	Moderate	Fast	Slow	Moderate	Fast
r	0.69	0.80	0.83	0.60	0.73	0.80	0.66	0.72	0.76	0.61	0.72	0.83
nBias	-0.09	-0.05	-0.02	-0.12	-0.07	-0.06	-0.13	-0.10	-0.06	-0.13	-0.06	-0.01
nRMSE	0.60	0.54	0.52	0.66	0.55	0.51	0.60	0.52	0.52	0.59	0.55	0.49
Sample mean ($g\ m^{-3}$)	0.47	0.47	0.50	0.46	0.51	0.50	0.44	0.48	0.51	0.45	0.53	0.54
Sample STD ($g\ m^{-3}$)	0.42	0.42	0.45	0.44	0.42	0.43	0.39	0.41	0.42	0.38	0.43	0.45
Domain mean ($g\ m^{-3}$)	0.52	0.50	0.51	0.52	0.55	0.53	0.51	0.53	0.54	0.51	0.56	0.54
Domain STD ($g\ m^{-3}$)	0.30	0.33	0.36	0.30	0.34	0.35	0.30	0.32	0.33	0.29	0.33	0.36

Zigzag

Speed Category	Slow	Moderate	Fast
r	0.62	0.74	0.37
nBias	-0.13	0.02	0.20
nRMSE	0.80	0.76	1.27
Sample mean ($g\ m^{-3}$)	0.35	0.42	0.47
Sample STD ($g\ m^{-3}$)	0.41	0.46	0.52
Domain mean ($g\ m^{-3}$)	0.40	0.41	0.40
Domain STD ($g\ m^{-3}$)	0.30	0.30	0.20

The zigzag vertical pattern shows a distinct behavior in which slope values do not systematically increase with flight speed. The number of valid CWC samples retained for the zigzag analysis ranges from 19410 at slow speed to 27617 at fast speed, pooled across all cases. Despite the larger number of valid samples at higher speeds, the zigzag pattern shows a close coupling between horizontal position and cloud-relative height. Each horizontal track corresponds to a prescribed cloud-base, mid-cloud, or cloud-top level, forming a stacked sampling loop. Increasing aircraft speed therefore increases the distance travelled along the same geometric patterns without changing the underlying vertical–horizontal structure. As a result, the trajectory continues to sample similar cloud-relative levels. In contrast, the level-leg, sine wave, and staircase patterns decouple horizontal position from sampled cloud-relative height, allowing increased speed to provide broader spatial sampling of the cloud field.

Overall, the sampling representativeness depends on both flight speed and trajectory geometry. While increased speed generally improves agreement for most vertical patterns through increasing spatial coverage, the constrained geometry of the zigzag configuration results in a less consistent response to increasing speed.

4.2 Representativeness of Cloud-Top and Cloud-Base Heights Across Sampling Strategies

The cloud-top and cloud-base conditions along the trajectory paths are further evaluated in Figure 7, which presents box plots of the differences between sampled and domain-mean cloud-top and cloud-base for all horizontal patterns and speed categories. The sampled cloud-base and cloud-top heights are calculated from the cloudy columns intersected by the aircraft-like trajectories, while the corresponding domain-mean values are obtained by averaging cloud-base and cloud-top heights across all cloudy columns within the model domain; clear columns are excluded from both calculations. Across the horizontal configurations, sampled cloud-top heights exhibit systematic negative differences, indicating that the cloud tops along the aircraft-like trajectories are generally lower than those over the full model domain. In contrast, cloud-base heights show substantially smaller differences relative to the domain mean, showing stronger agreement across configurations. This asymmetry is consistent with the cloud-field statistics summarized in Supplemental Materials (Table S1), which indicate greater variability in cloud-top height than in cloud-base height, as reflected by the larger standard deviation. These results suggest that the designed flight paths are more effective in capturing the lower cloud boundary, whereas the more heterogeneous cloud-top structure is less fully represented along the trajectories and therefore more susceptible to sampling stochasticity. The performance of the zigzag pattern is consistent with other horizontal configurations in terms of the negative tendencies for cloud-top height and relatively improved agreement for cloud base. This indicates that the zigzag geometry does not introduce a distinct systematic bias in boundary height itself. Rather, its effect is reflected more strongly in representativeness metrics of bulk CWC, as shown in Figure 6.

Differences among horizontal sampling patterns are comparatively secondary to the influence of flight speed. Across all patterns, discrepancies in both cloud-top and cloud-base heights decrease with increasing speed, with the fast-speed category exhibiting the smallest differences relative to the domain mean. At higher prescribed speeds, the trajectory covers a larger portion of each 10 min model field, reducing sensitivity to localized cloud gaps and cloud-edge variability. This greater spatial coverage improves agreement with the domain-mean cloud-boundary structure within the present sampling framework. Because the model field is held fixed within each 10 min interval, the observed speed dependence primarily reflects differences in spatial coverage rather than temporal sampling frequency or sample count. Horizontal sampling geometry has a comparatively smaller influence on boundary-height estimates.

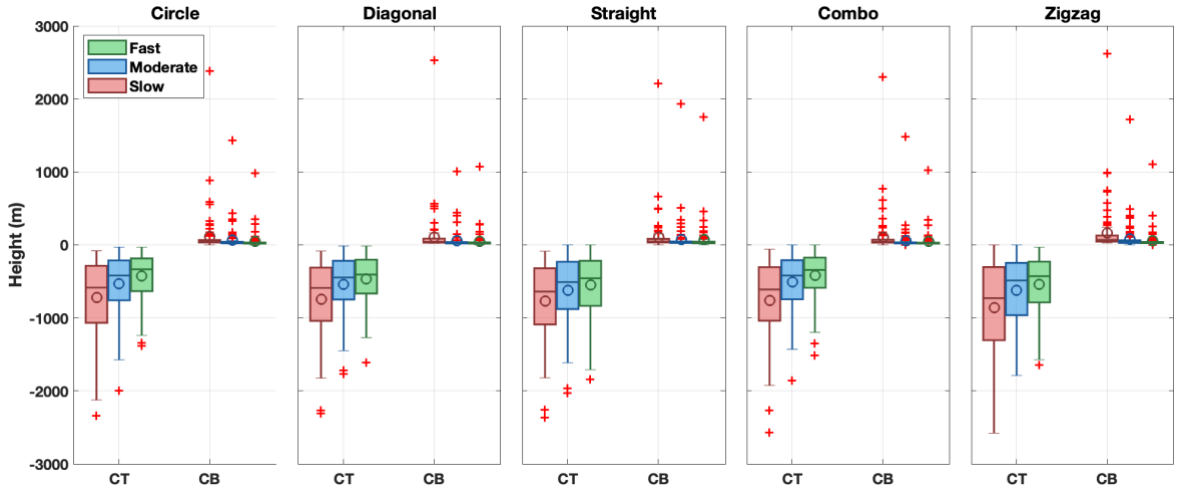


Figure 7: Box plots of differences between sampled and domain-mean cloud-top (CT) and cloud-base (CB) heights for five horizontal sampling patterns (circle, diagonal, straight, combo, and zigzag) and three flight speed categories (green for fast speed; blue for moderate speed; red for slow speed).

4.3 Vertical Profiles of Sampled CWC Across Speed Categories

The vertical profiles of sampled CWC obtained from designed aircraft trajectories using the level-leg, sine wave, staircase, and zigzag vertical sampling patterns under three speed categories are shown in Figure 8. For the level-leg, sine wave, and staircase profiles, results are averaged across all horizontal sampling patterns to isolate the effects of vertical sampling and flight speed, while the zigzag configuration is evaluated separately. Across all vertical patterns, the sampled profiles capture the primary structural characteristics of the domain-mean CWC, including the altitude and magnitude of the main cloud layer.

The correlation coefficient calculated over the full sampled altitude range shows distinct differences for each pattern. The level-leg profile yields correlations of 0.36, 0.21, and 0.15 for the slow, moderate, and fast speed categories, respectively. In contrast, the sine wave and staircase patterns show substantially weaker correlations with values ranging from –0.12 to 0.16 and –0.06 to 0.12, respectively. These reduced correlations partly reflect differences in the altitude ranges sampled by the vertical profiles and the greater variability in the upper cloud layers.

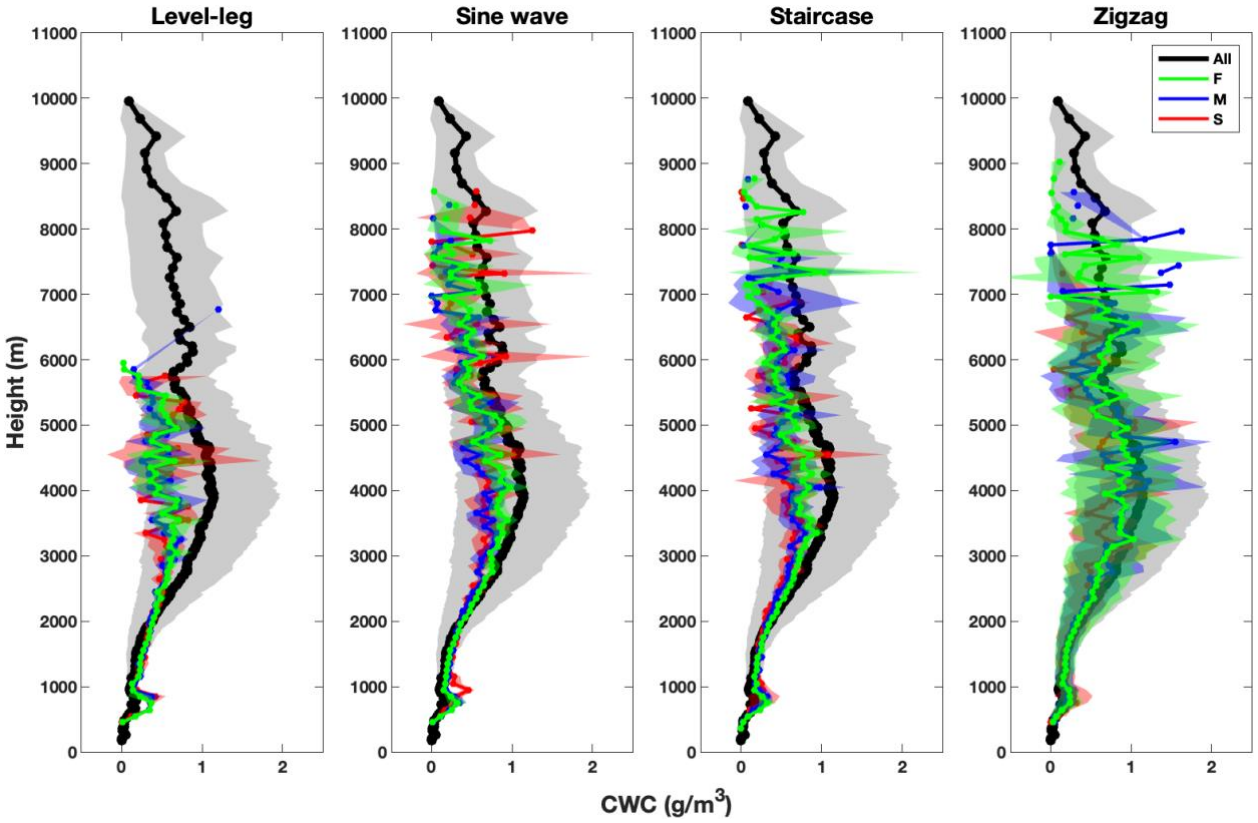


Figure 8: Vertical profiles of CWC sampled using four distinct vertical sampling patterns (level-leg, sine wave, staircase, and zigzag), shown in separate panels. Within each panel, the colored curves denote different flight-speed categories, while the black curve represents the domain-mean CWC profile computed over the full model domain. The shaded envelope indicates ±1 standard deviation of the domain CWC, providing a quantitative measure of the intrinsic vertical variability. For the level-leg, sine wave, and staircase profiles, results are averaged across the four horizontal sampling patterns; the zigzag configuration is shown separately.

Because the level-leg pattern does not extend into the upper cloud layers, the correlations were also calculated over the common altitude range of approximately 0 to 6000 m. Within this shared layer, the sine wave correlations are 0.48, 0.40, and 0.43 for the slow, moderate, and fast speed categories, respectively, while the staircase correlations are 0.32, 0.40, and 0.40. The zigzag configuration shows the highest correlations within this restricted range (0.42, 0.53, and 0.60 for slow, moderate, and fast speed, respectively). The higher correlations within the common altitude range indicate that part of the weaker full depth correlations for the sine wave and staircase profiles is associated with the additional upper-level variability included in those profiles.

Normalized error metrics remain consistent with this interpretation. The level-leg pattern shows larger normalized bias (1.56–1.81) and nRMSE (1.91–2.14), whereas the sine wave and staircase profiles exhibit smaller bias (0.66–0.96 for sine wave; 0.57–0.80 for staircase) and reduced nRMSE (1.47–1.56 and 1.32–1.48, respectively), indicating improved agreement due to broader vertical coverage. The zigzag profile yields intermediate normalized errors (0.82–1.39 for nBias; 1.60–2.05

for nRMSE) while maintaining the strongest correlations within the shared altitude range, likely related to its structured sequencing of cloud-relative levels, which enhances covariance within the sampled layer.

Across patterns, increasing flight speed generally improves agreement within the common altitude range. However, improvements are not uniform across the full cloud depths, indicating that while greater spatial coverage can reduce sensitivity to localized variability, vertical trajectory geometry and the inclusion of highly variable upper cloud layers remain primary controls on the representativeness of the domain-averaged vertical CWC distribution.

4.4 Sampling Performance Across Cloud-Fraction Categories

To examine whether sampling performance varies with cloud amount, the cases were grouped into four CF categories (0–25%, 25–50%, 50–75%, and 75–100%) based on the maximum CF among the 10-min model outputs within each simulated period. The four categories contain 39, 42, 7, and 3 cases, respectively. The correlation coefficients and regression slopes vary among the CF categories and sampling configurations (Table S2), but do not show a consistent monotonic change with increasing CF. For example, for the level-leg profile combined with the circle horizontal pattern, r ranges from approximately 0.76–0.86, 0.43–0.68, 0.38–0.74, and 0.61–0.82 across the four CF categories, respectively, depending on flight speed. The corresponding regression slopes likewise vary among CF categories rather than changing systematically with increasing CF. The relatively small number of cases in the two highest-CF categories may reduce the stability of the corresponding statistics. Detailed results across sampling configurations are provided in Figure S2.

5 Conclusion

This study evaluates the representativeness of aircraft sampling within the LASSO LES framework over the ARM SGP site, using CWC as the primary variable for assessing sampling performance. By prescribing different horizontal flight patterns, vertical sampling strategies, and flight speed categories, we examine how trajectory geometry influences the correspondence between aircraft-like measurements and LES domain-average cloud properties.

The results show that aircraft sampling representativeness depends primarily on vertical trajectory design and flight speed. For the level-leg, sine wave, and staircase configurations, increasing flight speed generally improves agreement with the layer-restricted domain mean by increasing the spatial extent sampled within each fixed model-output interval and reducing sensitivity to localized heterogeneity. Among the vertical strategies, the staircase pattern generally shows strong agreement with the domain mean across the sampling configurations, with relatively high correlations and small normalized bias. In the vertical-profile comparison, the level-leg pattern shows comparatively larger normalized errors, highlighting that correlation alone is not sufficient to characterize sampling representativeness.

The interpretation of sampling performance also depends on the vertical layer over which statistical metrics are computed. When correlations are calculated over the full sampled cloud layer, the sine wave and staircase profiles show reduced correlations relative to the level-leg case. However, this reduction is mainly associated with the inclusion of highly variable upper cloud layers. When the analysis is restricted to a common altitude range, correlations increase substantially and become comparable across patterns. This indicates that lower full-layer correlations are driven by enhanced vertical variability rather than inferior performance within the sampled altitude range. Cloud-boundary analysis shows that sampled cloud-top heights are generally lower than the domain mean, whereas cloud-base heights are more consistently captured. Increasing flight speed reduces both the bias and variability of cloud-boundary estimates. Differences among horizontal patterns are comparatively secondary to the influence of vertical trajectory design and flight speed.

Case subsets grouped by CF do not show a consistent monotonic dependence of sampling performance on cloud amount across the sampling configurations examined. The CF-stratified results therefore suggest that bulk cloud amount alone does not systematically determine sampling representativeness within the present analysis. Sampling performance may also be influenced by cloud-field structure, including cloud size, cloud spacing, and variability in cloud-base and cloud-top heights. Several limitations should be considered when interpreting these results. The present analysis does not systematically isolate the effects of trajectory scale or orientation relative to the mean wind, which may interact with cloud morphology and influence sampling performance. These factors were not independently varied in the current experimental design and therefore cannot be quantitatively isolated from the present set of simulations. The LES framework used here assumes a horizontally uniform lower boundary and therefore does not represent surface heterogeneity associated with land cover, soil moisture, or antecedent precipitation, all of which may further influence spatial cloud variability under real atmospheric conditions. The imposed LES large-scale forcing is also constant across the domain, which effectively neglects mesoscale variability in the background meteorology. Because the LES uses horizontally homogeneous external forcing and surface boundary conditions, heterogeneity not represented in the present framework could increase cloud-field variability and alter the sampling statistics.

Overall, this study provides a quantitative framework for interpreting aircraft-based cloud measurements relative to LES domain averages and for designing flight strategies for model–observation comparison studies. Within the present idealized framework, sampling representativeness is affected by vertical trajectory geometry and spatial coverage, with horizontal pattern exerting a smaller influence. Increasing speed reduces stochastic sampling variability, but systematic biases associated with geometric structure and vertical heterogeneity remain.

Future work should extend this framework to additional cloud regimes and explicitly incorporate time-evolving cloud fields to better represent realistic operational flight conditions. Sensitivity experiments that systematically vary flight duration and sampling interval would further clarify how spatial coverage and temporal sampling interact with trajectory geometry in determining sampling representativeness. The current analysis relies on simulations at 10-min temporal resolution, which

may limit the representation of shorter-timescale cloud variability. As a result, cloud evolution within these intervals is not represented, and the speed dependence primarily reflects differences in spatial coverage. Simulations with finer temporal resolution will enable a more detailed examination of sampling strategies. Applying higher-resolution model simulations would further support trajectory design studies by resolving finer-scale cloud structures. This study focuses on CWC as a proof-of-concept for establishing the sampling framework. Future applications can extend this methodology to additional cloud properties, including LWP and model-derived process rates, as well as to other cloud types. In addition, future work will extend this framework to aerosol sampling, evaluating sampling strategies and their representativeness along aircraft trajectories to improve model–observation comparisons of aerosol-cloud interactions.

Code and data availability

The LASSO simulation outputs used in this study are publicly available through the Atmospheric Radiation Measurement (ARM) Data Center via the LASSO browser: http://adc.arm.gov/lassobrowser. The simulations analyzed here correspond to the ARM LASSO shallow convection scenario at the Southern Great Plains (SGP) atmospheric observatory. The aircraft observations are from the ARM Aerial Facility Merged Value-Added Product (AAFMERGED), which provides integrated airborne measurements from historical G-1 aircraft field campaigns and is publicly available through the ARM Data Center at https://armgov.svcs.arm.gov/data/science-data-products/vaps/aafmerged. The analysis scripts used in this manuscript are publicly available at https://github.com/KkristineE/SGP-LES.

Supplement link

The link to the supplement will be included by Copernicus, if applicable.

Author contributions

JL performed the formal analysis, investigation, coding, and original draft preparation. JG and DRC contributed to the conceptualization and methodology. JG supervised the study. WIG provided data curation. JG, WIG, and DRC contributed to review and editing of the manuscript.

Competing interests

The authors declare that they have no conflict of interest.

Disclaimer

Copernicus Publications remains neutral with regard to jurisdictional claims made in the text, published maps, institutional affiliations, or any other geographical representation in this paper. While Copernicus Publications makes every effort to include appropriate place names, the final responsibility lies with the authors. Views expressed in the text are those of the authors and do not necessarily reflect the views of the publisher.

Acknowledgements

This work is supported by the U.S. Department of Energy, Office of Science, Office of Biological and Environmental Research, through the Established Program to Stimulate Competitive Research (DOE EPSCoR) under Award Number DE-SC0024161. Portions of the work were performed at Pacific Northwest National Laboratory (PNNL). Battelle Memorial Institute operates PNNL under contract DE-AC05-76RL01830. The Oak Ridge Leadership Computing Facility at the Oak Ridge National Laboratory is supported by the Office of Science of the U.S. Department of Energy under Contract No. DE-AC05-00OR22725. Computing resources for LASSO simulations were provided by the Atmospheric Radiation Measurement (ARM) user facility, with additional operational support from the Oak Ridge Leadership Computing Facility.

Financial support

JL, DRC, and JG were supported by the U.S. Department of Energy, Office of Science, Office of Biological and Environmental Research, through the Established Program to Stimulate Competitive Research (DOE EPSCoR) under Award Number DE-SC0024161. WIG was supported by the U.S. Department of Energy, Office of Science, Office of Biological and Environmental Research, through the Atmospheric Radiation Measurement (ARM) user facility.

Review statement

The review statement will be added by Copernicus Publications listing the handling editor as well as all contributing referees according to their status anonymous or identified.

References

Ackerman, T. P., & Stokes, G. M. (2003). The Atmospheric Radiation Measurement Program. Physics Today, 56(1), 38–44. https://doi.org/10.1063/1.1554135

595 Berg, L. K., Gustafson, W. I., Kassianov, E. I., & Deng, L. (2013). Evaluation of a Modified Scheme for Shallow Convection: Implementation of CuP and Case Studies. Monthly Weather Review, 141(1), 134–147. https://doi.org/10.1175/MWR-D-12-00136.1

Berg, L. K., & Kassianov, E. I. (2008). Temporal Variability of Fair-Weather Cumulus Statistics at the ACRF SGP Site.
600 Journal of Climate, 21(13), 3344–3358. https://doi.org/10.1175/2007JCLI2266.1

Brenguier, J., Bachalo, W. D., Chuang, P. Y., Esposito, B. M., Fugal, J., Garrett, T., Gayet, J., Gerber, H., Heymsfield, A., Kokhanovsky, A., Korolev, A., Lawson, R. P., Rogers, D. C., Shaw, R. A., Strapp, W., & Wendisch, M. (2013). In Situ Measurements of Cloud and Precipitation Particles. In M. Wendisch & J. Brenguier (Eds.), Airborne Measurements for
605 Environmental Research (1st ed., pp. 225–301). Wiley. https://doi.org/10.1002/9783527653218.ch5

Ceppi, P., & Nowack, P. (2021). Observational evidence that cloud feedback amplifies global warming. Proceedings of the National Academy of Sciences, 118(30), e2026290118. https://doi.org/10.1073/pnas.2026290118

610 D'Alessandro, J. J., McFarquhar, G. M., Stith, J. L., Diao, M., DeMott, P. J., McCluskey, C. S., Hill, T. C. J., Roberts, G. C., & Sanchez, K. J. (2023). An Evaluation of Phase, Aerosol-Cloud Interactions and Microphysical Properties of Single- and Multi-Layer Clouds Over the Southern Ocean Using in Situ Observations From SOCRATES. Journal of Geophysical Research: Atmospheres, 128(15), e2023JD038610. https://doi.org/10.1029/2023JD038610

615 Dorff, H., Ewald, F., Konow, H., Mech, M., Ori, D., Schemann, V., Walbröl, A., Wendisch, M., & Ament, F. (2025). Moisture budget estimates derived from airborne observations in an Arctic atmospheric river during its dissipation. Atmospheric Chemistry and Physics, 25(14), 8329–8354. https://doi.org/10.5194/acp-25-8329-2025

Fast, J. D., Bell, D. M., Kulkarni, G., Liu, J., Mei, F., Saliba, G., Shilling, J. E., Suski, K., Tomlinson, J., Wang, J., Zaveri,
620 R., & Zelenyuk, A. (2022). Using aircraft measurements to characterize subgrid-scale variability of aerosol properties near the Atmospheric Radiation Measurement Southern Great Plains site. Atmospheric Chemistry and Physics, 22(17), 11217–11238. https://doi.org/10.5194/acp-22-11217-2022

Fast, J. D., Berg, L. K., Feng, Z., Mei, F., Newsom, R., Sakaguchi, K., & Xiao, H. (2019). The Impact of Variable Land-
625 Atmosphere Coupling on Convective Cloud Populations Observed During the 2016 HI-SCALE Field Campaign. Journal of Advances in Modeling Earth Systems, 11(8), 2629–2654. https://doi.org/10.1029/2019MS001727

Field, P. R., & Furtado, K. (2016). How Biased Is Aircraft Cloud Sampling? *Journal of Atmospheric and Oceanic Technology*, *33*(1), 185–189. https://doi.org/10.1175/JTECH-D-15-0148.1

Gerber, H., Frick, G., Malinowski, S. P., Brenguier, J.-L., & Burnet, F. (2005). Holes and Entrainment in Stratocumulus. Journal of the Atmospheric Sciences, 62(2), 443–459. https://doi.org/10.1175/JAS-3399.1

Gerber, H., Frick, G., Malinowski, S. P., Jonsson, H., Khelif, D., & Krueger, S. K. (2013). Entrainment rates and microphysics in POST stratocumulus. Journal of Geophysical Research: Atmospheres, 118(21). https://doi.org/10.1002/jgrd.50878

Gryspeerdt, E., McCoy, D. T., Crosbie, E., Moore, R. H., Nott, G. J., Painemal, D., Small-Griswold, J., Sorooshian, A., & Ziemba, L. (2022). The impact of sampling strategy on the cloud droplet number concentration estimated from satellite data. Atmospheric Measurement Techniques, 15(12), 3875–3892. https://doi.org/10.5194/amt-15-3875-2022

Gustafson, WI, AM Vogelmann, X Cheng, S Endo, B Krishna, Z Li, T Toto, and H Xiao, 2018: Description of the LASSO Alpha 2 Release. Ed. by R. Stafford, DOE Atmospheric Radiation Measurement user facility, DOE/SC-ARM-TR-199, doi:10.2172/1376727.

Gustafson, W. I., Vogelmann, A. M., Li, Z., Cheng, X., Dumas, K. K., Endo, S., Johnson, K. L., Krishna, B., Fairless, T., & Xiao, H. (2020). The Large-Eddy Simulation (LES) Atmospheric Radiation Measurement (ARM) Symbiotic Simulation and Observation (LASSO) Activity for Continental Shallow Convection. Bulletin of the American Meteorological Society, 101(4), E462–E479. https://doi.org/10.1175/BAMS-D-19-0065.1

Gustafson, W., Vogelmann, A., Cheng, X., Endo, S., Krishna, B., Li, Z., Toto, T., Xiao, H., & Johnson, K. (2017). *LASSO Data Bundles* (p. 3 TB) [Dataset]. Atmospheric Radiation Measurement (ARM) Archive, Oak Ridge National Laboratory (ORNL), Oak Ridge, TN (US); ARM Data Center, Oak Ridge National Laboratory (ORNL), Oak Ridge, TN (United States). https://doi.org/10.5439/1342961

IPCC, 2013: *Climate Change 2013: The Physical Science Basis*. Contribution of Working Group I to the Fifth Assessment Report of the Intergovernmental Panel on Climate Change [Stocker, T. F., D. Qin, G.-K. Plattner, M. Tignor, S. K. Allen, J. Boschung, A. Nauels, Y. Xia, V. Bex, and P. M. Midgley (eds.)]. Cambridge University Press, Cambridge, United Kingdom and New York, NY, USA, 1535 pp

Katzwinkel, J., Siebert, H., Heus, T., & Shaw, R. A. (2014). Measurements of Turbulent Mixing and Subsiding Shells in Trade Wind Cumuli. *Journal of the Atmospheric Sciences*, *71*(8), 2810–2822. https://doi.org/10.1175/JAS-D-13-0222.1

Khairoutdinov, M. F., & Randall, D. A. (2003). Cloud Resolving Modeling of the ARM Summer 1997 IOP: Model Formulation, Results, Uncertainties, and Sensitivities. Journal of the Atmospheric Sciences, 60(4), 607–625. https://doi.org/10.1175/1520-0469(2003)060<0607:CRMOTA>2.0.CO;2

Krämer, M., Twohy, C., Hermann, M., Afchine, A., Dhaniyala, S., & Korolev, A. (2013). Aerosol and Cloud Particle Sampling. In M. Wendisch & J. Brenguier (Eds.), Airborne Measurements for Environmental Research (1st ed., pp. 303–341). Wiley. https://doi.org/10.1002/9783527653218.ch6

Kulkarni, G., Mei, F., Shilling, J. E., Wang, J., Reveggino, R. P., Flynn, C., Zelenyuk, A., & Fast, J. (2023). Cloud Condensation Nuclei Closure Study Using Airborne Measurements Over the Southern Great Plains. Journal of Geophysical Research: Atmospheres, 128(5), e2022JD037964. https://doi.org/10.1029/2022JD037964

Mather, J. H., & Voyles, J. W. (2013). The Arm Climate Research Facility: A Review of Structure and Capabilities. Bulletin of the American Meteorological Society, 94(3), 377–392. https://doi.org/10.1175/BAMS-D-11-00218.1

McFarquhar, G., Schmid, B., Korolev, A., Ogren, J. A., Russell, P. B., Tomlinson, J., Turner, D. D., & Wiscombe, W. (2011). Airborne Instrumentation Needs for Climate and Atmospheric Research. Bulletin of the American Meteorological Society, 92(9), 1193–1196. https://doi.org/10.1175/2011BAMS3180.1

McPherson, R. A., Fiebrich, C. A., Crawford, K. C., Kilby, J. R., Grimsley, D. L., Martinez, J. E., Basara, J. B., Illston, B. G., Morris, D. A., Kloesel, K. A., Melvin, A. D., Shrivastava, H., Wolfinbarger, J. M., Bostic, J. P., Demko, D. B., Elliott, R. L., Stadler, S. J., Carlson, J. D., & Sutherland, A. J. (2007). Statewide Monitoring of the Mesoscale Environment: A Technical Update on the Oklahoma Mesonet. Journal of Atmospheric and Oceanic Technology, 24(3), 301–321. https://doi.org/10.1175/JTECH1976.1

Mei, F., Comstock, J. M., Pekour, M. S., Fast, J. D., Gaustad, K. L., Schmid, B., Tang, S., Zhang, D., Shilling, J. E., Tomlinson, J. M., Varble, A. C., Wang, J., Leung, L. R., Kleinman, L., Martin, S., Biraud, S. C., Ermold, B. D., & Burk, K. W. (2024). Atmospheric Radiation Measurement (ARM) airborne field campaign data products between 2013 and 2018. Earth System Science Data, 16(11), 5429–5448. https://doi.org/10.5194/essd-16-5429-2024

Mei, F. and Gaustad, K.: ARM airborne field campaign data products aboard Gulfstream 159. Between 2013 and 2018, CACTI, ACE-ENA, HiScale, ACME-V, ACAPEX, GoAmazon, BBOP. Atmospheric Radiation Measurement (ARM) user facility, ARM Data Center: Oak Ridge, Tennessee, USA [data set], https://doi.org/10.5439/1999133 (last access: 20 August 2025), 2024, updated periodically.

Morrison, H., Thompson, G., & Tatarskii, V. (2009). Impact of Cloud Microphysics on the Development of Trailing Stratiform Precipitation in a Simulated Squall Line: Comparison of One- and Two-Moment Schemes. Monthly Weather Review, 137(3), 991–1007. https://doi.org/10.1175/2008MWR2556.1

Oue, M., Kollias, P., North, K. W., Tatarevic, A., Endo, S., Vogelmann, A. M., & Gustafson, W. I. (2016). Estimation of cloud fraction profile in shallow convection using a scanning cloud radar. Geophysical Research Letters, 43(20). https://doi.org/10.1002/2016GL070776

Passer, S. R., Witte, M. K., & Chuang, P. Y. (2025). Aircraft evaluation of MODIS cloud drop number concentration retrievals. Atmospheric Measurement Techniques, 18(15), 3819–3831. https://doi.org/10.5194/amt-18-3819-2025

Petzold, A., Formenti, P., Baumgardner, D., Bundke, U., Coe, H., Curtius, J., DeMott, P. J., Flagan, R. C., Fiebig, M., Hudson, J. G., McQuaid, J., Minikin, A., Roberts, G. C., & Wang, J. (2013). In Situ Measurements of Aerosol Particles. In M. Wendisch & J. Brenguier (Eds.), Airborne Measurements for Environmental Research (1st ed., pp. 157–223). Wiley. https://doi.org/10.1002/9783527653218.ch4

Sanchez-Marroquin, A., Hedges, D. H. P., Hiscock, M., Parker, S. T., Rosenberg, P. D., Trembath, J., Walshaw, R., Burke, I. T., McQuaid, J. B., & Murray, B. J. (2019). Characterisation of the filter inlet system on the FAAM BAe-146 research aircraft and its use for size-resolved aerosol composition measurements. *Atmospheric Measurement Techniques*, *12*(11), 5741–5763. https://doi.org/10.5194/amt-12-5741-2019

Savelyev, I., Thomas, L. N., Smith, G. B., Wang, Q., Shearman, R. K., Haack, T., Christman, A. J., Blomquist, B., Sletten, M., Miller, W. D., & Fernando, H. J. S. (2018). Aerial Observations of Symmetric Instability at the North Wall of the Gulf Stream. Geophysical Research Letters, 45(1), 236–244. https://doi.org/10.1002/2017GL075735

Schmid, B., Tomlinson, J. M., Hubbe, J. M., Comstock, J. M., Mei, F., Chand, D., Pekour, M. S., Kluzek, C. D., Andrews, E., Biraud, S. C., & McFarquhar, G. M. (2014). The DOE ARM Aerial Facility. Bulletin of the American Meteorological Society, 95(5), 723–742. https://doi.org/10.1175/BAMS-D-13-00040.1

Schneider, T., Lan, S., Stuart, A., & Teixeira, J. (2017). Earth System Modeling 2.0: A Blueprint for Models That Learn From Observations and Targeted High-Resolution Simulations. *Geophysical Research Letters*, *44*(24). https://doi.org/10.1002/2017GL076101

Schumann, U., Fahey, D. W., Wendisch, M., & Brenguier, J. (2013). Introduction to Airborne Measurements of the Earth Atmosphere and Surface. In M. Wendisch & J. Brenguier (Eds.), Airborne Measurements for Environmental Research (1st ed., pp. 1–5). Wiley. https://doi.org/10.1002/9783527653218.ch1

Schutgens, N., Tsyro, S., Gryspeerdt, E., Goto, D., Weigum, N., Schulz, M., & Stier, P. (2017). On the spatio-temporal representativeness of observations. *Atmospheric Chemistry and Physics*, *17*(16), 9761–9780. https://doi.org/10.5194/acp-17-9761-2017

Shin, H. H., Xue, L., Li, W., Firl, G., D'Amico, D. F., Muñoz-Esparza, D., Ek, M. B., Chu, Y., Wang, Z., Gustafson, W. I., & Vogelmann, A. M. (2021). Large-Scale Forcing Impact on the Development of Shallow Convective Clouds Revealed From LASSO Large-Eddy Simulations. Journal of Geophysical Research: Atmospheres, 126(20), e2021JD035208. https://doi.org/10.1029/2021JD035208

Sisterson, D. L., Peppler, R. A., Cress, T. S., Lamb, P. J., & Turner, D. D. (2016). The ARM Southern Great Plains (SGP) Site. Meteorological Monographs, 57, 6.1-6.14. https://doi.org/10.1175/AMSMONOGRAPHS-D-16-0004.1

Stevens, B., Ament, F., Bony, S., Crewell, S., Ewald, F., Gross, S., Hansen, A., Hirsch, L., Jacob, M., Kölling, T., Konow, H., Mayer, B., Wendisch, M., Wirth, M., Wolf, K., Bakan, S., Bauer-Pfundstein, M., Brueck, M., Delanoë, J., … Zinner, T. (2019). A High-Altitude Long-Range Aircraft Configured as a Cloud Observatory: The NARVAL Expeditions. Bulletin of the American Meteorological Society, 100(6), 1061–1077. https://doi.org/10.1175/BAMS-D-18-0198.1

Stevens, B., Moeng, C.-H., Ackerman, A. S., Bretherton, C. S., Chlond, A., De Roode, S., Edwards, J., Golaz, J.-C., Jiang, H., Khairoutdinov, M., Kirkpatrick, M. P., Lewellen, D. C., Lock, A., Müller, F., Stevens, D. E., Whelan, E., & Zhu, P. (2005). Evaluation of Large-Eddy Simulations via Observations of Nocturnal Marine Stratocumulus. *Monthly Weather Review*, *133*(6), 1443–1462. https://doi.org/10.1175/MWR2930.1

Thompson, G., & Eidhammer, T. (2014). A Study of Aerosol Impacts on Clouds and Precipitation Development in a Large Winter Cyclone. Journal of the Atmospheric Sciences, 71(10), 3636–3658. https://doi.org/10.1175/JAS-D-13-0305.1

Thompson, G., Field, P. R., Rasmussen, R. M., & Hall, W. D. (2008). Explicit Forecasts of Winter Precipitation Using an Improved Bulk Microphysics Scheme. Part II: Implementation of a New Snow Parameterization. Monthly Weather Review, 136(12), 5095–5115. https://doi.org/10.1175/2008MWR2387.1

Vogelmann, A. M., McFarquhar, G. M., Ogren, J. A., Turner, D. D., Comstock, J. M., Feingold, G., Long, C. N., Jonsson, H. H., Bucholtz, A., Collins, D. R., Diskin, G. S., Gerber, H., Lawson, R. P., Woods, R. K., Andrews, E., Yang, H.-J., Chiu, J. C., Hartsock, D., Hubbe, J. M., … Toto, T. (2012). Racoro Extended-Term Aircraft Observations of Boundary Layer Clouds. *Bulletin of the American Meteorological Society*, *93*(6), 861–878. https://doi.org/10.1175/BAMS-D-11-00189.1

Wagner, T. J., Turner, D. D., Berg, L. K., & Krueger, S. K. (2013). Ground-Based Remote Retrievals of Cumulus Entrainment Rates. Journal of Atmospheric and Oceanic Technology, 30(7), 1460–1471. https://doi.org/10.1175/JTECH-D-12-00187.1

Wang, Z., French, J., Vali, G., Wechsler, P., Haimov, S., Rodi, A., Deng, M., Leon, D., Snider, J., Peng, L., & Pazmany, A. L. (2012). Single Aircraft Integration of Remote Sensing and In Situ Sampling for the Study of Cloud Microphysics and Dynamics. *Bulletin of the American Meteorological Society*, *93*(5), 653–668. https://doi.org/10.1175/BAMS-D-11-00044.1

Wang, Z., & Sassen, K. (2001). Cloud Type and Macrophysical Property Retrieval Using Multiple Remote Sensors. Journal of Applied Meteorology, 40(10), 1665–1682. https://doi.org/10.1175/1520-0450(2001)040<1665:CTAMPR>2.0.CO;2

Wendisch, M., & Brenguier, J. (Eds.). (2013). Airborne Measurements for Environmental Research: Methods and Instruments (1st ed.). Wiley. https://doi.org/10.1002/9783527653218

Wendisch, M., Pilewskie, P., Bohn, B., Bucholtz, A., Crewell, S., Harlow, C., Jäkel, E., Schmidt, K. S., Shetter, R., Taylor, J., Turner, D. D., & Zöger, M. (2013). Atmospheric Radiation Measurements. In M. Wendisch & J. Brenguier (Eds.), Airborne Measurements for Environmental Research (1st ed., pp. 343–411). Wiley. https://doi.org/10.1002/9783527653218.ch7

Wilson Kemsley, S., Ceppi, P., Andersen, H., Cermak, J., Stier, P., & Nowack, P. (2024). A systematic evaluation of high-cloud controlling factors. Atmospheric Chemistry and Physics, 24(14), 8295–8316. https://doi.org/10.5194/acp-24-8295-2024

Zelinka, M. D., Myers, T. A., McCoy, D. T., Po-Chedley, S., Caldwell, P. M., Ceppi, P., Klein, S. A., & Taylor, K. E. (2020). Causes of Higher Climate Sensitivity in CMIP6 Models. Geophysical Research Letters, 47(1), e2019GL085782. https://doi.org/10.1029/2019GL085782

Zhang, H., Su, T., Zheng, Y., & Li, Z. (2024). First Assessment of Cloud-Land Coupling in LASSO Large-Eddy Simulations. Geophysical Research Letters, 51(14), e2024GL109774. https://doi.org/10.1029/2024GL109774

Zhang, Y., & Klein, S. A. (2010). Mechanisms Affecting the Transition from Shallow to Deep Convection over Land: Inferences from Observations of the Diurnal Cycle Collected at the ARM Southern Great Plains Site. Journal of the Atmospheric Sciences, 67(9), 2943–2959. https://doi.org/10.1175/2010JAS3366.1

Zhang, Y., & Klein, S. A. (2013). Factors Controlling the Vertical Extent of Fair-Weather Shallow Cumulus Clouds over Land: Investigation of Diurnal-Cycle Observations Collected at the ARM Southern Great Plains Site. Journal of the Atmospheric Sciences, 70(4), 1297–1315. https://doi.org/10.1175/JAS-D-12-0131.1

Zheng, X., Dong, X., Xi, B., Logan, T., & Wang, Y. (2024). Distinctive aerosol–cloud–precipitation interactions in marine boundary layer clouds from the ACE-ENA and SOCRATES aircraft field campaigns. Atmospheric Chemistry and Physics, 24(18), 10323–10347. https://doi.org/10.5194/acp-24-10323-2024

Zhu, L., Lu, C., Chen, J., Wang, Y., He, X., Li, J., Wu, X., & Wu, S. (2024). Aircraft Observations Reveal the Relationship Between Cumulus Entrainment Rate and Aerosol Loading. Geophysical Research Letters, 51(19), e2024GL110881. https://doi.org/10.1029/2024GL110881